# Single-Laser Krypton Tagging Velocimetry Investigation of Supersonic Air and $N_2$ Boundary-Layer Flows over a Hollow Cylinder in a Shock Tube

Muhammad A. Mustafa, David Shekhtman, and Nick J. Parziale*
*Stevens Institute of Technology, Mechanical Engineering, Castle Point on Hudson, Hoboken, New Jersey 07030, USA*

(Received 20 March 2019; revised manuscript received 20 May 2019; published 6 June 2019)

In this paper, we investigate the boundary-layer profiles that form over a sharp, hollow cylinder in supersonic air and $N_2$ flows with a krypton tagging velocimetry (KTV) single-laser scheme. The supersonic flows are generated by the passage of the primary shock wave over the model in the Stevens shock tube. The experiments are performed in two gas mixtures doped with Kr: 99% $N_2$/1% Kr, to model $N_2$, and 75% $N_2$/20% $O_2$/5% Kr, to model air. The experimental setup allows us to vary the pressure and Reynolds number from 3–25 kPa and $1.5 \times 10^5$ to $1.5 \times 10^6$ $m^{-1}$, respectively, while the Mach number is kept fixed at 1.7. The static temperature and pressure (but not the velocity) are representative of typical large-scale high-enthalpy hypersonic impulse facilities. The KTV data points over the hollow cylinder are mapped to corresponding wall-normal locations above a flat plate, which enables comparison with the similarity solution for compressible boundary-layer flow. Agreement between the similarity solution and experimental results is excellent. Relative to previous two-laser KTV schemes, the single-laser approach used in this work has the advantage of being simpler and more cost effective, but it has a higher laser-energy requirement, 10 mJ/pulse in these experiments. Single-laser KTV is implemented by increasing the energy of the write-laser pulse to a sufficient level such that the Kr becomes partially ionized via a $(2 + 1)$ resonance-enhanced, multiphoton ionization (REMPI) process with an excitation wavelength of 212.6 nm. The write step records the fluorescence that results primarily from the spontaneous emission from the two-photon excitation. After a prescribed delay, the read step records the fluorescence that results from the transitions that follow the recombination process. The signal-to-noise ratio (SNR) is sufficient to extract velocity profiles from single-shot, shock-tube experiments. Two-photon absorption cross-section calculations and emission spectra are presented to justify the chosen excitation wavelength and support our understanding of the Kr excitation and emission scheme.

DOI: 10.1103/PhysRevApplied.11.064013

## I. INTRODUCTION

High-speed flow is characterized by various complex phenomena such as shock waves, turbulence, chemical reactions, and nonequilibrium effects. These complex phenomena and their interactions have aerothermodynamic design implications for high-speed vehicles. To optimize the design of such vehicles, it is necessary to generate predictive computational tools that are capable of modeling high-speed flow physics. To this end, nonintrusive, off-surface experimental techniques are required to assess computational-model performance while they are being developed and applied to canonical flows; additionally, advanced diagnostics serve as a check on computational-model performance during the vehicle design stage.

Many variables are of interest when comparing experimental and computational results; velocity is one such variable [1]. Ubiquitous particle-based measurement techniques such as particle-image velocimetry (PIV) [2,3] rely on the assumption that the tracer particles travel identically with the flow. However, the particle response time can be inadequate in low-density, high-Mach-number flows with short timescales because of particle slip due to high Knudsen number [4]. This represents a fundamental limitation of particle-based techniques because the slip condition at the particle surface reduces response time. Several researchers [5–7] have examined the response of particles to shock waves in an effort to quantify particle response time. Williams *et al.* [8] suggest that "particle frequency response analyses based solely on shock response tests may well have overestimated the response to turbulence." Measurement of velocity fluctuations in high-speed, turbulent boundary layers is an example that brings the particle-response-time limitation to bear. Lowe *et al.* [9] assert that "[s]trong evidence exists that experimental data gathered in high speed flows using particle-based techniques exhibit significant particle lag effects on magnitudes of turbulence quantities." This assertion was based

*nick.parziale@gmail.com

 

on an experimental laser-Doppler velocimetry (LDV) campaign in a Mach 2.0 turbulent boundary layer, and the authors made particle-lag corrections to address discrepancies in their data. Recent PIV work by Brooks *et al.* [10] found that particle-lag effects are more pronounced in the turbulence quantities associated with the wall-normal velocity than the streamwise velocity. This is because the wall-normal velocity fluctuation spectrum is flatter (has more high-frequency content) than its streamwise counterpart.

An attractive alternative to particle-based techniques is tagging velocimetry. Tagging velocimetry [11] is typically performed in gases by tracking the fluorescence of a native, seeded, or synthesized gas. Its advantage over PIV techniques in high-speed facilities is that it is not limited by timing issues associated with tracer injection [12] or reduced particle response at Knudsen and Reynolds numbers [4] characteristic of high-speed wind tunnels. Methods of tagging velocimetry include the VENOM [13–17], APART [18–20], RELIEF [21–25], FLEET [26, 27], STARFLEET [28], PLEET [29], NO [30–34], argon [35], iodine [36,37], sodium [38], acetone [39–41], NH [42], and the hydroxyl group techniques [43–46], among others [47–52].

To recreate high-speed flow conditions for model and vehicle development, various facilities are used depending on the requirements [53]. In this work, the focus is on impulse facilities, some of which are able to reproduce total flow enthalpy for short periods of time [54]. These facilities, which include shock and expansion tunnels, reproduce the flow velocity which can be important for research into mixing [55], thermochemical and fluid-mechanical interactions [56–58], and boundary-layer instability [59–61] and transition [62–64].

Challenges with making measurements in these facilities include vibration; short test times; experimental timing; harsh pre- and postflow conditions; and, in the case of particle-based techniques, particle injection [65]. Particle-based applications of velocimetry in impulse facilities include the impulsively started flow over a cylinder in a shock tube [66], PIV in shock tunnels [12], and shocked particle drag measurements [67]. Tagging velocimetry has also been applied in impulse facilities. Hydroxyl tagging velocimetry (HTV) was used to make measurements behind the bow shock wave that formed on a model in a shock tube [68]. Additionally, NO has been used as a tagging tracer to measure the freestream flow [34] and flow over test articles in reflected-shock tunnels [31].

In this paper, we focus on a version of tagging velocimetry called krypton tagging velocimetry (KTV) as applied to flow over a sharp, hollow cylinder after the passage of the primary shock wave in the Stevens shock tube. Experiments are conducted in air and in $N_2$ that is doped with Kr. The experimental setup is described, namely, a simplified single-laser version of KTV that is justified by two-photon absorption cross-section calculations and emission spectra. Finally, results are presented from experiments conducted over a range of static thermodynamic conditions that are similar to larger-scale impulse hypersonic facilities to demonstrate KTV utility. These experimental results are compared to similarity solutions for compressible boundary-layer flow with excellent agreement.

## II. SINGLE-LASER EXCITATION SCHEME FOR KTV

In this work, we focus on the use of Kr as a tracer for tagging velocimetry, which was first suggested by Mills *et al.* [69] and Balla and Everhart [70]. The key to the use of Kr as a tracer species for diagnostics is the two-photon transitions in the range of approximately 190–220 nm that are accessible with commercially available optics and laser systems. To date, KTV has been demonstrated by globally seeding high-speed $N_2$ flows with 1% Kr and air flows with 5% Kr. Applications include (i) an underexpanded jet (first KTV demonstration) [71], (ii) mean and fluctuating turbulent boundary-layer profiles in a Mach 2.7 flow [72], (iii) more than 20 simultaneous profiles of streamwise velocity and velocity fluctuations in a Mach 2.8 shock-wave/turbulent boundary-layer interaction [73], and (iv) the freestream of the large-scale AEDC Hypervelocity Tunnel 9 at Mach 10 and Mach 14 [74]. In these experiments, the researchers used a pulsed-dye laser to perform the write step at 214.7 nm to both form a write line and photosynthesize the metastable Kr tracer; after a prescribed delay, an additional pulsed dye laser was used to reexcite the metastable Kr tracer to track displacement. Recently, simplified KTV schemes were developed and demonstrated in an underexpanded jet [75], where either (a) a pulsed-dye laser was used for the write step and a simple continuous-wave laser diode was used for the read step or (b) successive images of the fluorescence from a single dye-laser pulse were used. In this work, a single-laser scheme is used to make the KTV measurements.

Following the transitions marked in blue and red in the energy-level diagram in Fig. 1 along with the relevant transition data in Table I (labeled as A, B, C, etc.), the single-laser KTV scheme is performed as follows:

1. **Write Step:** Excite krypton atoms with a pulsed-tunable laser to form the tagged tracer through a $(2+1)$ resonance-enhanced, multiphoton ionization (REMPI) process [76–80]. Firstly, two-photon excitation of $4p^6(^1S_0) \rightarrow 5p[1/2]_0$ (two 212.6 nm photons, transition A) and subsequent one-photon ionization (one 212.6-nm photon, transition C). Fluorescence for the write step is recorded primarily from the decay to the resonance state $5p[1/2]_0 \rightarrow 5s[3/2]_1^o$ (758.7 nm, transition B). Minor fluorescence contributions from transitions E and F, resulting from the recombination process (transition D) [81,82] are

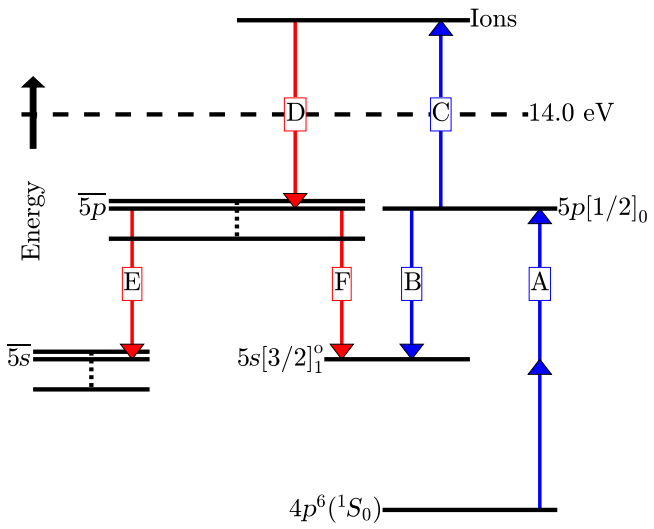


FIG. 1. Energy diagram with Racah $nl[K]_J$ notation for a single-laser, $(2+1)$ REMPI KTV scheme with excitation at 212.6 nm and successive camera gating (no read laser). Transition details are given in Table I. States $\overline{5p}$ and $\overline{5s}$ represent the numerous $5p$ and $5s$ states (tabulated in Table II) that are created by the recombination process. Transitions E and F represent the numerous transitions in the $5p$-$5s$ band. 14.0 eV marks the ionization limit of Kr.

also recorded. The position of the write line is marked by gated imaging of the laser-induced fluorescence (LIF) from these transitions, recorded with a camera positioned normal to the flow. The emission spectrum of this step is shown in black in Fig. 2.

2. **Read Step:** After a prescribed delay, record the displacement of the tagged krypton by gated imaging of the LIF from the residual $5p[1/2]_0 \rightarrow 5s[3/2]_1^o$ (758.7 nm) transition B, in addition to other transitions E and F resulting from the recombination process D. At this step, the fluorescences from transitions E and F dominate those of B. The emission spectrum of this step is shown in red or blue in Fig. 2.

Emission spectra are recorded to investigate the $(2+1)$ REMPI process and extent of the ionization of the fluorescing Kr atoms during the write and read steps. The hypothesis is that if the spectra indicate transitions other than the $5p[1/2]_0 \rightarrow 5s[3/2]_1^o$ (758.7 nm) transition, the Kr atoms are at least partially ionized. As a result of the partially ionized Kr population, the fluorescence observed during the read step would be the result of the spontaneous emission from the by-products of the Kr recombination process [81,82]. This process occurs at a longer timescale than spontaneous emission in the absence of ionization, thus enabling the tagged Kr atoms to be imaged with sufficient signal-to-noise ratio (SNR) during the read step without the need for a read laser.

The optical setup to record the spectra is identical to that used to record the data for the boundary-layer measurements (Fig. 5) with two exceptions. The experiments are conducted in quiescent flow, and, instead of imaging the fluorescing Kr atoms directly onto a camera, the Kr fluorescence is imaged onto the slit of an Oriel MS257, 25-cm spectrograph. The spectra are imaged with a Princeton Instruments PIMAX-4 (PM4-1024i-HR-FG-18-P46-CM) camera. The lens used is a Nikon NIKKOR 24–85-mm f/2.8-4D with a 0.5-in. lens tube positioned at the spectrograph exit. This experimental setup is calibrated with a Kr pen lamp (Newport 6031).

The emission spectrum at three time increments after the write-laser pulse is presented in Fig. 2. We denote the time after the write-laser pulse as $\Delta t$, with the spectra recorded at $\Delta t = 0$ ns being representative of the write step and the spectra recorded at $\Delta t = 500$ ns or $\Delta t = 1000$ ns being representative of the read step. The experiments are performed with a 212.6-nm wavelength, 3-mJ energy pulse in a 5-torr, 99% $N_2$/1% Kr mixture. The 758.7-nm transition dominates at $\Delta t = 0$ ns, corresponding to transition B in Fig. 1. From this, we conclude that the write-step fluorescence is dominated by the spontaneous emission from the $5p[1/2]_0 \rightarrow 5s[3/2]_1^o$ (758.7 nm) transition. For the spectra recorded at $\Delta t = 500$ ns and $\Delta t = 1000$ ns, many transitions are observed that are consistent with spontaneous emission from Kr atoms in the $5p$ states (Table II). From this, we conclude that the read-step fluorescence is due to the spontaneous emission from the by-products of the Kr recombination process. We should note that we record spectra with 80-nm windows (e.g., 750–830 nm in Fig. 2) over a broad domain in the 400–850-nm range and

TABLE I. Relevant NIST atomic spectra database lines data, such that the labels match Fig. 1, with Racah $nl[K]_J$ notation.

| Transition[a] | $\lambda_{air}$ (nm) | Nature | $A_{ki}$ (1/s) | $E_i$ (cm$^{-1}$) | $E_k$ (cm$^{-1}$) | Lower level | Upper level |
|---|---|---|---|---|---|---|---|
| A | 212.56 | Two-photon | not applicable | 0 | 94 092.8626 | $4s^24p^6, {}^1S_0$ | $5p[1/2]_0$ |
| B | 758.74 | Single-photon | $4.3 \times 10^7$ | 80916.7680 | 94092.8626 | $5s[3/2]_1^o$ | $5p[1/2]_0$ |
| C | 212.56 | Single-photon | not applicable | 94 092.8626 | 112 914.433 | $5p[1/2]_0$ | Kr ions |
| E/F[b] | 750–830 | Single-photon | $10^6$–$10^7$ | 80 000 | 90 000 | $\overline{5s}$ | $\overline{5p}$ |

[a]Transition D is not listed because it is not an atomic-level transition. It represents the recombination process.
[b]Entries in this row represent ranges and order of magnitude estimates since E and F in Fig. 1 represent numerous transitions in the $5p$-$5s$ band.

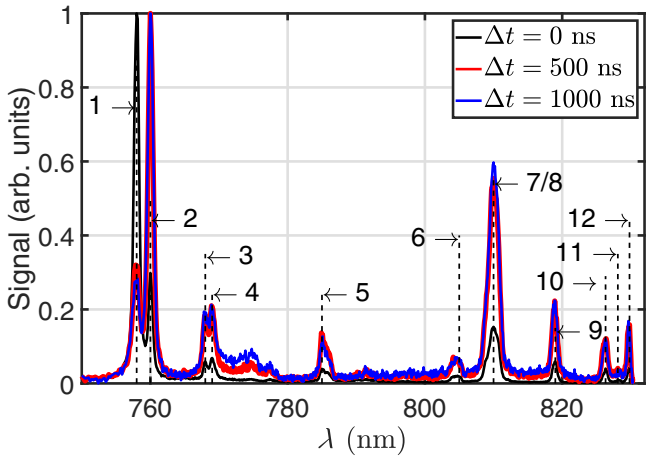


FIG. 2. Emission spectra for the (2 + 1) REMPI process using λ = 212.6-nm excitation in a 99% $N_2$/1% Kr mixture. Atomic data for each line are presented in Table II. Intensities are normalized by maximum intensity at each time step.

record little or no signal outside of the 750–830-nm range. The emission results we present in Fig. 2 are consistent with those in the literature for ionized Kr; for example, see the relative intensities (Table I) and energy-level diagram (Fig. 5) of Shiu and Biondi [81]. Additionally, we note that while maintaining laser intensity, detuning the laser wavelength off of the 212.6-nm resonance by a few picometers resulted in the complete loss of fluorescence. From this, we conclude that we are not photoionizing other constituents in the gas mixtures.

To understand the timescales of the tagged Kr lines, experiments are conducted where camera exposures of Kr fluorescence are recorded at successive times after the write-laser pulse, each with a 30-ns gate width. The optical setup for this series of experiments is identical to that in the boundary-layer measurements (Fig. 5), except the experiments are performed in a quiescent flow. Results

TABLE II. Atomic data for krypton spectra using λ = 212.6-nm two-photon excitation in $N_2$, with Racah $nl[K]_J$ notation. The line numbers correspond to Fig. 2.

| Line | $\lambda_{air}$ (nm) | Upper level | Lower level |
|---|---|---|---|
| 1 | 758.74 | $5p[1/2]_0$ | $5s[3/2]_1^o$ |
| 2 | 760.15 | $5p[3/2]_2$ | $5s[3/2]_2^o$ |
| 3 | 768.52 | $5p'[1/2]_0$ | $5s'[1/2]_1^o$ |
| 4 | 769.45 | $5p[3/2]_1$ | $5s[3/2]_2^o$ |
| 5 | 785.48 | $5p'[1/2]_1$ | $5s'[1/2]_0^o$ |
| 6 | 805.95 | $5p'[3/2]_1$ | $5s'[1/2]_0^o$ |
| 7 | 810.44 | $5p[5/2]_2$ | $5s[3/2]_2^o$ |
| 8 | 811.29 | $5p[5/2]_3$ | $5s[3/2]_2^o$ |
| 9 | 819.01 | $5p[3/2]_2$ | $5s[3/2]_1^o$ |
| 10 | 826.32 | $5p'[3/2]_2$ | $5s'[1/2]_1^o$ |
| 11 | 828.11 | $5p'[1/2]_1$ | $5s'[1/2]_1^o$ |
| 12 | 829.81 | $5p[3/2]_1$ | $5s[3/2]_1^o$ |

are presented in Fig. 3 for both 99% $N_2$/1% Kr and 75% $N_2$/20%$O_2$/5% Kr mixtures. To estimate what the fluorescence signal behavior would be in the absence of ionization, we present a simple model. The population of the excited state $5p[1/2]_0$, $N$, is governed by $N = N_0 \exp(-Rt)$, where $N_0$ is the integration constant and $R = A_{ij} + Q$ is the sum of the Einstein coefficient, $A_{ij}$, for transition B in Fig. 1 and the quenching rate, $Q$, which is estimated from Ref. [83]. The camera signal, $F$, at time $t$ after the pulse, is then $F = \int_t^{t+\Delta t} NA_{ij}\,dt + n$, where $\Delta t$ is the camera gate time and $n$ is the noise level in the image [84]. Carrying out the integration gives

$$F = (F_0 - n)\exp(-R(t - t_0)) + n, \tag{1}$$

where $F_0$ is the initial signal at $t = t_0$. The initial condition, $F_0$, for Eq. (1) is prescribed as the signal count at the end of the laser pulse. The results in Fig. 3 show that the experiment and Eq. (1) are in reasonable agreement up to 20 ns after the laser pulse, after which Eq. (1) predicts the signal to drop into the noise within 100 ns of the write-laser pulse. Note that in Fig. 3, the signal in air is higher in the beginning because of the extra krypton (5% vs 1% in $N_2$); however, the signal decays faster in air because of the quenching due to $O_2$, and after a certain point (approximately 800 ns), the signal in air becomes lower than the signal in $N_2$.

The effects of pressure and mixture composition on the fluorescence signal are shown as Fig. 4. For a given gas mixture, the signal at the write step is higher for higher pressure cases because of increased Kr density. However,

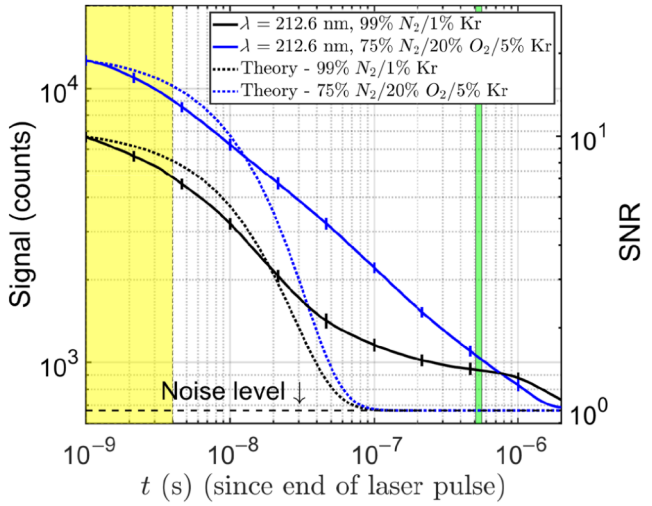


FIG. 3. Fluorescence curves for 99% $N_2$/1% Kr and 75% $N_2$/20% $O_2$/5% Kr at 5 torr for the (2 + 1) REMPI process using λ = 212.6-nm excitation. The yellow and green regions are representative of the camera gate for the write step and read step, respectively. The theory corresponds to Eq. (1). Vertical bars denote uncertainty.

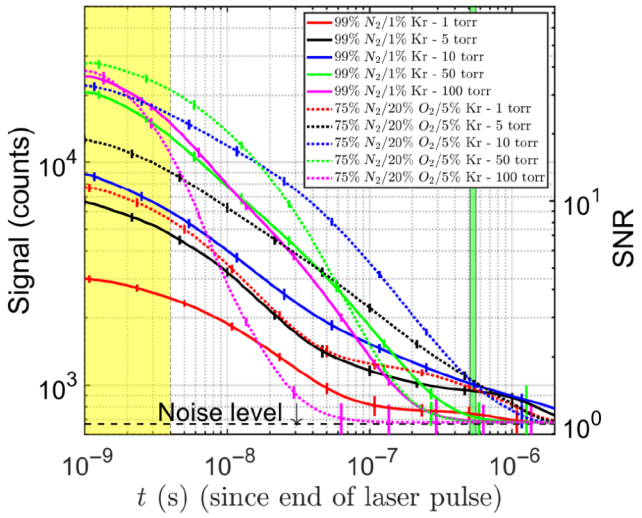


FIG. 4. Fluorescence curves for 99% $N_2$/1% Kr and 75% $N_2$/20% $O_2$/5% Kr at various pressures for the $(2+1)$ REMPI process using $\lambda = 212.6$-nm excitation. The yellow and green regions are representative of the camera gate for the write step and read step, respectively. Vertical bars denote uncertainty.

for the same high pressure cases, the signal at the read step may be lower because the quenching rate increases with pressure.

From the emission spectra (Fig. 2) and the time-resolved fluorescence results (Figs. 3 and 4), we conclude that the lifetime of the fluorescence signal is extended because the write-laser pulse is intense enough to partially ionize the Kr and the recombination process is slow enough to enable a single-laser KTV technique.

The write-pulse energy requirement of the KTV scheme in this work is higher than that of previous schemes. Previous KTV schemes require two lasers: one for the write step and photosynthesis of the metastable state tracer and one for the reexcitation from the metastable state on the read step. In this work, $(2+1)$ REMPI and the recombination process are responsible for the long lifetime of the Kr fluorescence. For context on energy requirements, the previous two-laser scheme was able to write many lines with relatively low energy, as in the work of Mustafa *et al.* [73], where 20 lines with 350 $\mu$J/line were used to investigate a Mach 3 shock-wave/turbulent boundary-layer interaction over a $20 \times 20$-mm domain. In this work, we have only a single line because of energy requirements, but the setup is simpler, and, as is discussed later, is demonstrated over a broad range of conditions in Kr-doped $N_2$ and air. We note that in the work of Mustafa and Parziale [75], a scheme is presented where a simple, inexpensive diode laser was used for the read step in place of a complex dye-laser setup, and more work with the laser-diode strategy is forthcoming.

## III. CROSS-SECTION CALCULATIONS

In this section, we estimate Kr two-photon cross sections to justify the choice of excitation wavelength following the works of Lambropoulos [85] and Khambatta *et al.* [86,87]. To a first approximation, we assume that a larger two-photon cross section will result in more effective $(2+1)$ REMPI and thus yield a larger fluorescence signal for the single-laser scheme used in this work.

The $5p[1/2]_0$ (212.6 nm) energy level [rather than the $5p[3/2]_2$ (214.7 nm) energy level] is used in this work because of its apparently larger two-photon cross section. This observation appears to have first been made by Richardson *et al.* [88], where they observed an appreciable increase in the fluorescence signal when implementing Kr-planar laser induced fluorescence, noting that they were likely not operating their laser in the ionization regime.

The two-photon excitation rate, $W$, is proportional to the cross section, $\sigma^{(2)}$, and the square of the photon flux, $\Phi = I/(h\nu_L)$, and can be written as

$$W = \sigma^{(2)}\Phi^2. \tag{2}$$

Clearly, an increase in the cross section would increase the number of atoms in the higher-energy state that can then be ionized with an additional photon. Plank's constant, the incident laser intensity, and the incident laser frequency are $h$, $I$, and $\nu_L$, respectively. Following Lambropoulos [85], the two-photon cross section can be calculated as

$$\sigma^{(2)} = (2\pi)^3\alpha^2\omega_L^2 g(2\omega_L)|M_{fg}|^2, \tag{3}$$

where $\alpha$ is the fine structure constant and $\omega_L$ is the laser angular frequency. The line-shape function for two-photon excitation, $g(2\omega_L)$, is written on resonance as

$$g(2\omega_L = \omega_T) = \frac{2\sqrt{\ln(2)/\pi}}{\sqrt{2(\Delta\omega_L)^2 + (\Delta\omega_T)^2}}, \tag{4}$$

assuming the transition (Doppler broadened) and laser linewidths are Gaussians, and the full width at half maxima are $\Delta\omega_L$ and $\Delta\omega_T$ for the laser and transition, respectively.

The term $M_{fg}$ represents the sum of the contributions to the two-photon cross section by individual channels with a ground state $g$, an intermediate state $i$, and a final state $f$. Following Lambropoulos [85], $M_{fg}$ may be written as

$$M_{fg} = \sum_i \frac{\langle f|r^\lambda|i\rangle\langle i|r^\lambda|g\rangle}{\omega_i - \omega_g - \omega_L}, \tag{5}$$

where the sum is over all possible intermediate states. Here, $\langle i|r^\lambda|g\rangle$ represents the matrix element for the transition from the ground state to the intermediate state and, similarly, $\langle f|r^\lambda|i\rangle$ represents the matrix element for the

transition from the intermediate state to the final state. Following Khambatta *et al.* [86,87], the matrix elements are calculated for linearly polarized light as

$$|\langle i|r^{\lambda}|g\rangle|^2 = (2J_i+1)\begin{pmatrix} J_i & 1 & J_g \\ -M_i & 0 & M_g \end{pmatrix}^2 \frac{3hc_0^3\epsilon_0}{2e^2}\frac{A_{ig}}{\omega_{ig}^3}, \quad (6)$$

and

$$|\langle f|r^{\lambda}|i\rangle|^2 = (2J_f+1)\begin{pmatrix} J_f & 1 & J_i \\ -M_f & 0 & M_i \end{pmatrix}^2 \frac{3hc_0^3\epsilon_0}{2e^2}\frac{A_{fi}}{\omega_{fi}^3}. \quad (7)$$

Here, $J$ and $M$ are the angular momentum and magnetic quantum numbers, respectively. The squared quantity in parentheses is the Wigner 3j symbol. The physical constants $h$, $c_0$, $\epsilon_0$, and $e$ are Planck's constant, speed of light in a vacuum, permittivity of free space, and electron charge, respectively. Finally, $A$ and $\omega$ are the Einstein coefficient and angular frequency of the transitions, respectively. This formulation gives the matrix elements in Eqs. (6) and (7) in units of $m^2$, assuming all physical constants are in meters-kilograms-seconds. We note that the results in Eqs. (6) and (7) are equivalent to those in Khambatta *et al.* [87] Sec. IV, Eq. (6), although their units are different.

In this work, the single-path approximation of Khambatta *et al.* [86] is used, where the summation over all intermediate states in Eq. (5) is reduced to a single term by considering only the resonance state, $5s[3/2]_1^0$, as the intermediate. Table III shows the two-photon cross sections for the $5p[1/2]_0$ and $5p[3/2]_2$ energy levels of krypton, corresponding to two-photon excitation using $\lambda = 212.6$ nm and $\lambda = 214.7$ nm, along with the corresponding atomic data used in the calculation. Furthermore, the magnetic quantum numbers are $M_g = M_i = M_f = 0$ for both energy levels because the laser is linearly polarized [89], and $\Delta\omega_L = 8.48 \times 10^9$ rad/s.

Our calculations indicate that the $5p[1/2]_0$ level has a larger two-photon cross section than the $5p[3/2]_2$ level. This cross-section calculation, along with observations in our lab and others [88], justifies the use of the 212.6-nm excitation wavelength for the single-laser scheme in this work via efficient (2 + 1) REMPI.

TABLE III. Two-photon cross sections and relevant atomic data. $W_{g1}$ and $W_{1f}$ represent the Wigner 3-j symbols for the ground-to-intermediate and intermediate-to-final transitions, respectively.

| Level (–) | $\lambda$ (nm) | $\lambda_{gi}$ (nm) | $\lambda_{fi}$ (nm) | $\Delta\omega_T$ $s^{-1}$ | $g(2\omega_L = \omega_T)$ s | $J_g$ (–) | $J_1$ (–) | $J_f$ (–) | $A_{ig}$ $(s^{-1})$ | $A_{fi}$ $(s^{-1})$ | $\omega_{ig}$ $(s^{-1})$ | $\omega_{fi}$ $(s^{-1})$ | $W_{ig}$ (–) | $W_{fi}$ (–) | $\sigma^{(2)}$ $(cm^4\ s)$ |
|---|---|---|---|---|---|---|---|---|---|---|---|---|---|---|---|
| $5p[1/2]_0$ | 212.56 | 123.58 | 758.74 | $2.40 \times 10^{10}$ | $3.50 \times 10^{-11}$ | 0 | 1 | 0 | $2.98 \times 10^8$ | $4.31 \times 10^7$ | $1.52 \times 10^{16}$ | $2.48 \times 10^{15}$ | $(-\sqrt{\frac{1}{3}})$ | $(-\sqrt{\frac{1}{3}})$ | $6.00 \times 10^{-46}$ |
| $5p[3/2]_2$ | 214.70 | 123.58 | 819.00 | $2.38 \times 10^{10}$ | $3.53 \times 10^{-11}$ | 0 | 1 | 2 | $2.98 \times 10^8$ | $8.94 \times 10^6$ | $1.52 \times 10^{16}$ | $2.29 \times 10^{15}$ | $(-\sqrt{\frac{1}{3}})$ | $(+\sqrt{\frac{2}{15}})$ | $3.16 \times 10^{-46}$ |

## IV. FACILITY AND EXPERIMENTAL SETUP

In this section, we give an overview of the experimental setup. The goal of these experiments is to demonstrate single-laser KTV in an impulse environment at static temperatures and pressures similar to those of a high-enthalpy impulse hypersonic facility. To this end, we present measurements in the quasisteady flow behind the primary

shock wave in the Stevens shock tube over a hollow cylinder.

The laser setup in this work is considerably simpler than that of previous KTV techniques. The write-laser system is a frequency doubled Quanta Ray Pro-350 Nd:YAG laser and a frequency tripled Sirah PrecisionScan Dye Laser (DCM dye, DMSO solvent). The Nd:YAG laser pumps the dye laser with 1000 mJ/pulse at a wavelength of 532 nm. The dye laser is tuned to output a 637.7-nm beam and frequency tripling (Sirah THU 205) of the dye-laser output results in a 212.6-nm beam, with 10-mJ energy, 1350-MHz linewidth, and 7-ns pulse width at a repetition rate of 10 Hz. The write beam is focused into the test section with a 200-mm-focal-length, fused-silica lens. The beam fluence and spectral intensity at the waist are $43 \times 10^3$ J/cm$^2$ and $4.6 \times 10^3$ W/(cm$^2$ Hz), respectively. Additionally, we present data with sufficient SNR 15 mm away from the focal point where the beam fluence and spectral intensity are 310 J/cm$^2$ and 33 W/(cm$^2$ Hz), respectively. We note here that the fluences and intensities are significantly higher than those in past KTV experiments with a two-laser setup.

The intensified CCD camera used for all experiments is a Princeton Instruments PIMAX-4 (PM4-1024i-HR-FG-18-P46-CM) with the dual image feature (DIF) enabled. The lens used is a Nikon NIKKOR 24-85mm f/2.8-4D in "macro" mode that is positioned approximately 150 mm from the write and read location. The camera gate opens twice: first, for 5 ns immediately following the write-laser pulse and, second, at a prescribed delay time of 500 ns for 50 ns to capture the residual fluorescence. The relative differences in gate width are chosen to address write/read ghosting issues while using the DIF with a short interframe delay. That is, the write image intensity is high and bleeding into the read image for longer values of the write-image gate width. The "phosphor decay time" of the P46 phosphor screen proves to be appropriate in this application. The specified ghosting value for a 500-ns interframe delay is 10%. The choice of 500-ns interframe delay is made to balance competing goals in tagging velocimetry: (i) a longer delay is sought to reduce the error in the measurement in the usual way per Eq. (17); (ii) a shorter delay is sought to freeze as much of the fluid motion as possible (e.g., a 1-$\mu$s delay results in freezing structures on the order of 1 MHz or slower); and (iii) a shorter delay is sought for KTV because for higher-pressure cases, the SNR is too low to make consistent measurements. Figures 3 and 4 show that at about 1 $\mu$s, the SNR is too low for higher-pressure cases.

A schematic of the measurement location in the Stevens shock tube is shown in Fig. 5. Optical access is provided by three fused-silica windows near the end of the tube. The operation of the shock tube is initiated by a diaphragm-piercing mechanism, consisting of a solenoid and a plunger. Three pressure transducers (see Fig. 6) are

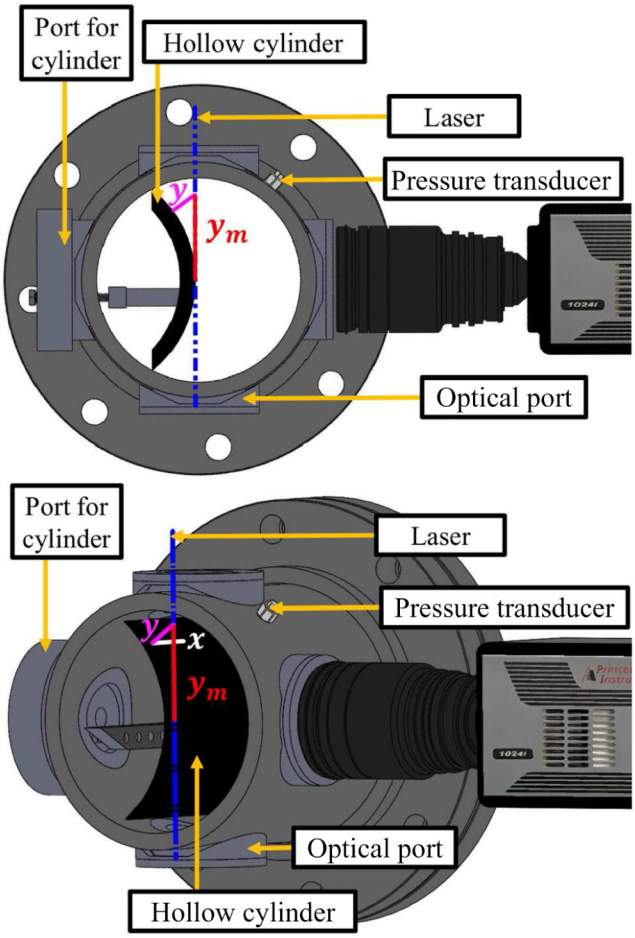


FIG. 5. Schematic of the test article in the shock tube. Top: Front view. Flow direction and $x$ (streamwise) coordinate are into the paper and along the surface of the cylinder. Bottom: Isometric view. $y$ and $y_m$ are as in Fig. 8.

installed along the length of the tube, the most downstream of which is at the measurement location (marked as "Pressure Transducer" in Fig. 5). There is also an additional port used to fill the driven section with gas mixtures. The experiments in this work are performed over a sectioned hollow cylinder with a sharp leading edge installed at the test location. The measurements are made in the $x$-$y_m$ coordinate system shown in Fig. 5 and are subsequently mapped to the $x$-$y$ coordinate system, as shown later. Figure 6 shows sample pressure traces from experiments in $N_2$ in both $x$-$t$ and $P$-$t$ space, indicating a useful test time of approximately 1 ms.

The timing of the experiment is designed to keep the laser at its operating temperature. As Fig. 7 shows, the laser and shock tube are controlled via pulse delay generators (PDG) and signal conditioners and amplifiers (used for signal addition and inversion). The diaphragm rupture timing is set to a delay after the write-laser flashlamp pulse following experiment activation. The delay is chosen such

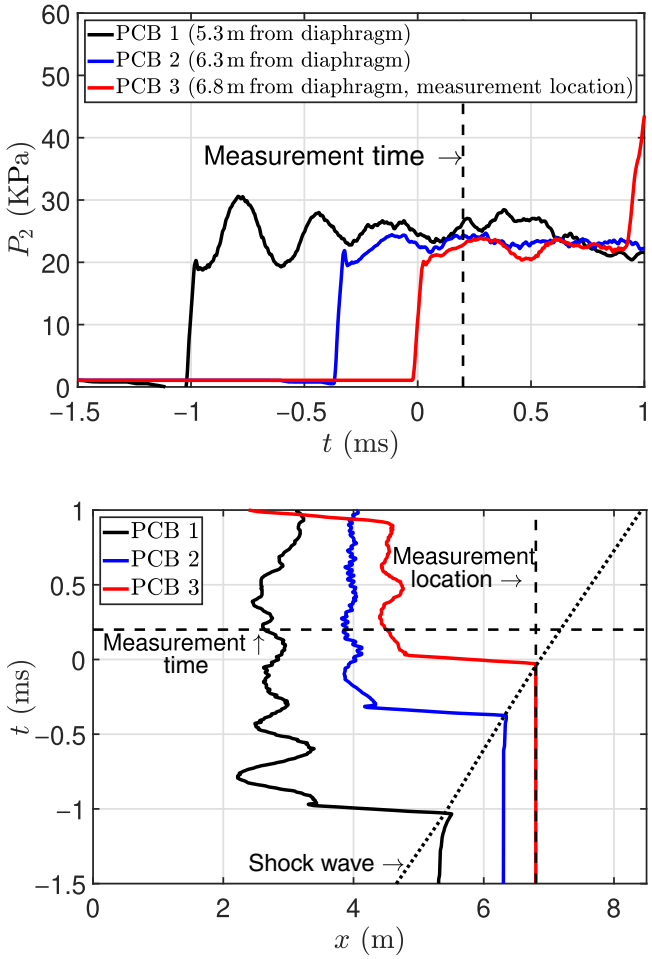


FIG. 6. Representative pressure traces. Data correspond to shot 169 in Table V. Top: *P*-*t* space. Bottom: *x*-*t* space.

that the laser and camera can be triggered upon arrival of the primary shock wave at the pressure transducer marked as "Pressure Transducer" in Fig. 5. This timing scheme keeps the laser system on an 8–12-Hz operation, which is close enough to specification for proper laser operation. In this setup, the laser timing dictates the shock tube timing, which is practical for developmental purposes in the lab. However, this timing strategy might not work in larger-scale shock tubes and tunnels, where there may be a 1–2-s delay between experiment initiation and the rupture of the primary diaphragm. With a conventional 10-Hz Nd:YAG/dye-laser setup like the one used in this work, less laser power would be available if a delay on the order of 1 s were introduced into this timing scheme. However, advanced laser technology might serve to alleviate this concern, in addition to significantly increasing the repetition rate. Data in the literature suggest that the write step could be performed by ultrafast lasers [88] or a tunable form of a burst-mode laser [90].

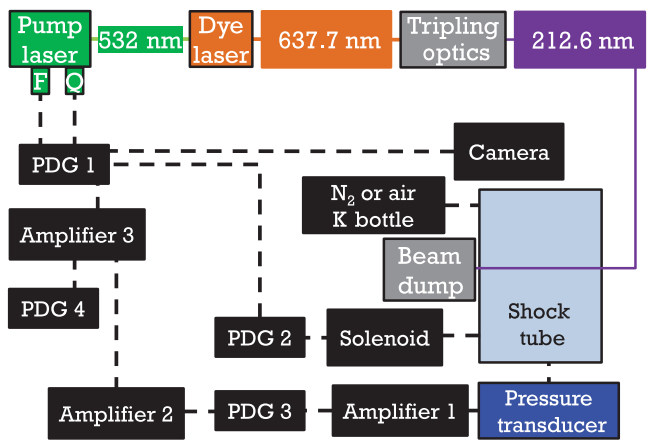


FIG. 7. Laser setup and timing for the Stevens shock tube.

The boundary-layer measurements are made on a sectioned, sharp-leading-edge hollow cylinder. In place of a flat plate, a cylindrical geometry is chosen because the write-laser beam could be propagated tangentially to the test article. This setup effectively increases the resolution near the wall by stretching the boundary layer and also reduces the effects of laser ablation on the test article surface.

The write laser excites Kr atoms on a line approximately tangent to the cylinder and the camera captures the projected image of the line, $y_m$, and its displacement (sketch in Fig. 8). The locations of tagged Kr atoms on this cylinder are mapped to corresponding wall-normal points, $y$, over a flat plate to transform the curved-surface problem into a flat-plate problem for comparison to the similarity

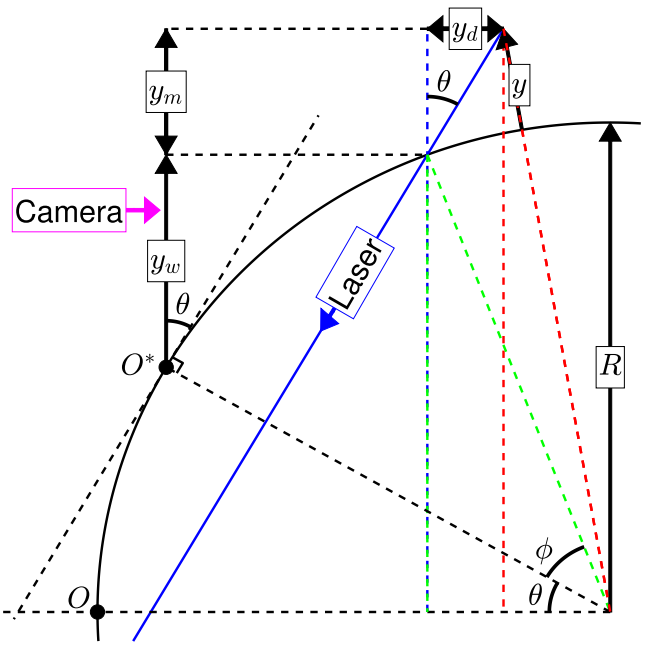


FIG. 8. Exaggerated sketch of the cylindrical surface (flow direction and streamwise coordinate, $x$, are out of the paper) and direction of laser propagation.

solution. The sketch in Fig. 8 is useful in the calculation of the mapped wall-normal location, $y$, as a function of the measurement distance $y_m$ (the quantity measured from camera images). The radius of the cylinder is $R$, the angular offset from the true apogee, $O$, is $\theta$, and the wall location from the observed apogee, $O^*$, is $y_w$. The derivation of the mapping expression for $y$ from $y_m$ uses this geometry, beginning with the green and red triangles drawn in the sketch. From the green triangle, a relationship between $\theta$ and $\phi$ is obtained as

$$\sin(\theta+\phi) = \frac{R\sin(\theta)+y_w}{R}. \tag{8}$$

Solving Eq. (8) for $\phi$ gives

$$\phi = \arcsin\left(\frac{R\sin(\theta)+y_w}{R}\right) - \theta. \tag{9}$$

To find the height of the red triangle, the distance $y_d$ is found via

$$y_d = \tan(\theta) y_m. \tag{10}$$

Applying the Pythagorean theorem to the red triangle yields the final expression for the wall-normal distance,

$$y = \sqrt{[R\cos(\theta+\phi)-y_d]^2 + [R\sin(\theta)+y_m+y_w]^2} - R. \tag{11}$$

Figure 9 shows the effects of $y_w$ and $\theta$ on the mapping from $y_m$ to $y$. The field of view of the current camera setup allows for a maximum $y_m$ of approximately 20 mm. Importantly, it is observed that the effect of $\theta$ is small until about 20°, but the effects of $y_w$ are significant. In these experiments $R = 84$ mm (size 6 pipe), $y_w \sim 0$–2 mm, and $\theta \sim 0°$.

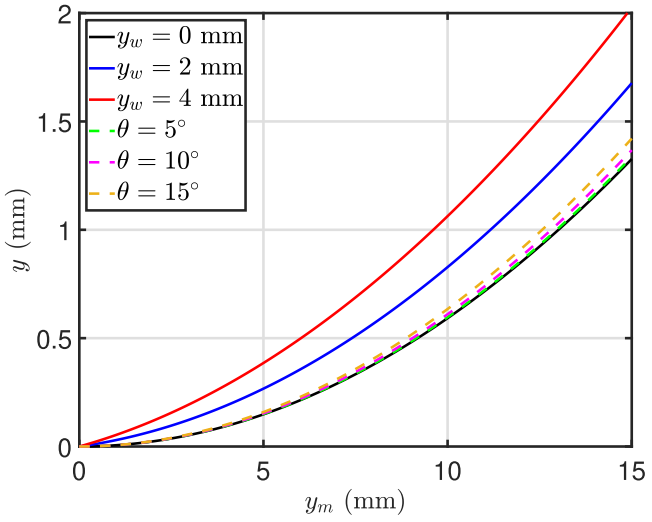


FIG. 9. Effect of $\theta$ and $y_w$ on mapping to flat-plate wall-normal location, $y$, as defined in Fig. 8.

## V. RUN CONDITIONS AND SIMILARITY SOLUTION FOR COMPRESSIBLE, LAMINAR BOUNDARY-LAYER FLOW

In these experiments, two gas mixtures are used in the driven section: 75% $N_2$/20% $O_2$/5% Kr to model air and 99% $N_2$/1% Kr to model $N_2$. The driver gas in all cases is helium. The pressure ratio between the driver and driven sections is kept fixed at $P_4/P_1 = 380$, with both sections starting at room temperature, $T_4 = T_1 \sim 298$ K. This fixes the primary shock wave speed, which nominally fixes the post-shock-wave (state-2) temperature ($T_2$), velocity ($u_2$), and Mach number ($M_2$) with varying pressure ($P_2$) and density ($\rho_2$). This experimental design enables a sweep of unit-Reynolds numbers from $1\times10^5$ to $1\times10^6$ m$^{-1}$ with nominally fixed temperature and velocity. The run conditions are presented in Tables IV and V, calculated with Cantera [91] and the Shock and Detonation toolbox [92]. The inputs for these calculations are the initial pressure, $P_1$, in the driven section (state 1); the primary shock wave speed (as measured by pressure transducers); and the gas composition.

In addition, the similarity solution for a compressible boundary layer over a flat plate is used as a basis for comparison to the KTV results mapped by Eq. (11). Following White [93], the equation governing momentum for a compressible, laminar boundary-layer flow over a flat plate is

$$(Cf'')' + ff'' = 0 \tag{12}$$

and the equation governing energy is

$$(Cg')' + Prfg' = -PrC(\gamma-1)M_2^2 f''^2. \tag{13}$$

Here, $f' = u/u_2$, $g = \rho_2/\rho = T/T_2$, $C = \rho\mu/\rho_2\mu_2$, and the derivatives are with respect to the similarity variable $\eta = (\sqrt{u_2}\int_0^y \rho dy)/\sqrt{2\rho_2\mu_2 x}$. Following Kuehl [94], $C$ is evaluated using Sutherland's law as

$$C = \frac{C_\mu\sqrt{T_2}}{\mu_2}\frac{\sqrt{g}}{g+(S/T_2)} = C_0\frac{\sqrt{g}}{g+C_1}, \tag{14}$$

where $C_\mu$ and $S$ are given in Table VI.

With this formulation, Eqs. (12) and (13) become

$$f''' = \frac{g'f''}{g+C_1} - \frac{g'f''}{2g} - \frac{ff''(g+C_1)}{C_0\sqrt{g}} \tag{15}$$

and

$$g'' = \frac{g'^2}{g+C_1} - \frac{g'^2}{2g} - Pr(\gamma-1)M_2^2 f''^2 - \frac{Prfg'(g+C_1)}{C_0\sqrt{g}}. \tag{16}$$

The boundary conditions are $f(\eta=0) = f'(\eta=0) = 0$, $g(\eta=0) = T_w/T_2$, and $f'(\eta\to\infty) = g(\eta\to\infty) = 1$.

TABLE IV. Experimental conditions for 75% $N_2$/20% $O_2$/5% Kr driven gas mixture and helium as driver gas.

| Shot | $Re_2^{\text{unit}}$ | $M_2$ | $P_2$ | $T_2$ | $\rho_2$ | $u_2$ | $M_s$ | $u_s$ |
|---|---|---|---|---|---|---|---|---|
| (–) | ($m^{-1}$) | (–) | (kPa) | (K) | ($kgm^{-3}$) | ($ms^{-1}$) | (–) | ($ms^{-1}$) |
| 163 | $1.56 \times 10^5$ | 1.76 | 2.65 | 1410 | 0.007 | 1230 | 4.58 | 1520 |
| 162 | $3.80 \times 10^5$ | 1.74 | 6.30 | 1370 | 0.018 | 1200 | 4.47 | 1480 |
| 159 | $7.67 \times 10^5$ | 1.74 | 12.6 | 1370 | 0.035 | 1190 | 4.46 | 1480 |
| 157 | $1.15 \times 10^6$ | 1.74 | 19.0 | 1380 | 0.053 | 1200 | 4.48 | 1490 |

The KTV measurements are made at $x = 43 \pm 3$ mm from the leading edge. Figure 10 shows representative temperature, density, and velocity profiles calculated using the similarity solution for the conditions in shot 169 in Table V.

## VI. DATA REDUCTION AND UNCERTAINTY ESTIMATE

In this section, we discuss how the data are reduced and we estimate the uncertainty of the KTV measurements. To process the KTV exposures, the line centers are found in the following way:

(1) Crop the image to an appropriate field of view.
(2) Apply a two-dimensional Wiener adaptive-noise removal filter.
(3) Convert the images to double precision numbers and normalize the intensity to fall in the range of 0–1.
(4) Apply the Gaussian peak-finding algorithm from O'Haver [95] to find the line center for the top row using the read line in the top row of each image as an initial guess.
(5) Proceeding from the top down, apply the Gaussian peak-finding algorithm from O'Haver [95] to find the line center for each row using the line center location immediately above as the initial guess.

No binning of the data is performed and a vertical and horizontal calibration length-scale (51.32 pixels/mm) is taken in the $x$-$y_m$ plane prior to the experiments.

Error bars for the KTV measurements are calculated in the same fashion as that of Zahradka *et al.* [72] as

$$\widetilde{U} = \sqrt{\left(\widetilde{\Delta x}\frac{\partial U}{\partial \Delta x}\right)^2 + \left(\widetilde{\Delta t}\frac{\partial U}{\partial \Delta t}\right)^2 + \left(v'_{\text{RMS}}\frac{\partial U}{\partial y}\Delta t\right)^2}, \tag{17}$$

where uncertainty estimates of a variable are indicated with a tilde. The uncertainty in the measured displacement distance, $\widetilde{\Delta x}$, of the tracer is estimated as 10 $\mu$m, from the 95% confidence bound on the write and read locations from the Gaussian fits. The uncertainty in time, $\widetilde{\Delta t}$, is estimated to be the camera gate width, 50 ns, which causes fluorescence blurring as considered in Bathel *et al.* [33]. The third term in Eq. (17) is uncertainty in streamwise velocity due to the wall-normal flow in the $x$-$y$ plane. This formulation is taken from Hill and Klewicki [96] and Bathel *et al.* [33]. The wall-normal fluctuations used in Eq. (17) ($v'_{\text{RMS}}$) are conservatively estimated to be 10% of the edge velocity.

## VII. RESULTS AND DISCUSSION

In this section, single-shot KTV measurements and similarity-solution calculations are presented and discussed for the Kr-doped air and $N_2$ experiments. In Figs. 11 and 12, we present results for each case at four unit Reynolds numbers, increasing top to bottom, with three plots in one box for each experiment. Corresponding flow conditions are listed in Tables IV and V. For each experiment, the plots on the left are the superposed, unmapped "write" and "read" KTV images, both of which are intensity normalized prior to superposition. The field of view of KTV measurements in these figures is approximately 20 mm. The plots in the center for each case are the superposed, mapped (cylinder to a flat plate) write and read KTV images, both of which are intensity normalized prior to superposition. For each case, the plots on the right show the similarity solution in blue and the KTV velocity profile in black with error bars in red as derived from Eq. (17).

The agreement between the KTV derived velocity profiles and the similarity solutions is excellent in Figs. 11 and 12. Because of our experimental design, the edge Mach

TABLE V. Experimental conditions for 99% $N_2$/1% Kr driven gas mixture and helium as driver gas.

| Shot | $Re_2^{\text{unit}}$ | $M_2$ | $P_2$ | $T_2$ | $\rho_2$ | $u_2$ | $M_s$ | $u_s$ |
|---|---|---|---|---|---|---|---|---|
| (–) | ($m^{-1}$) | (–) | (kPa) | (K) | ($kgm^{-3}$) | ($ms^{-1}$) | (–) | ($ms^{-1}$) |
| 165 | $3.90 \times 10^5$ | 1.72 | 6.01 | 1300 | 0.016 | 1220 | 4.37 | 1510 |
| 166 | $7.71 \times 10^5$ | 1.73 | 12.3 | 1340 | 0.031 | 1250 | 4.42 | 1550 |
| 168 | $1.15 \times 10^6$ | 1.73 | 18.2 | 1330 | 0.047 | 1250 | 4.39 | 1540 |
| 169 | $1.54 \times 10^6$ | 1.73 | 24.5 | 1340 | 0.063 | 1240 | 4.41 | 1540 |

TABLE VI. Constants for Sutherland's viscosity law.

| Gas (–) | $C_\mu$ (Pa s K$^{1/2}$) | $S$ (K) |
|---|---|---|
| Air | $1.458 \times 10^{-6}$ | 110.4 |
| $N_2$ | $1.407 \times 10^{-6}$ | 111 |

number is constant, so we observe that the boundary-layer thickness is reduced with increasing Reynolds number; this follows the typical scaling of compressible-boundary-layer thickness as $\delta \propto M^2/\sqrt{Re}$ [93]. The KTV derived velocity profiles are collapsed by normalizing the profile by the edge velocity and plotting against the similarity variable in Fig. 13. The similarity variable is $\eta = \left[\sqrt{u_2}\int_0^y \rho(y)dy\right]/\sqrt{2\rho_2\mu_2 x}$, where the density profile, $\rho(y)$, is calculated from the similarity solution. In Fig. 13, there is a weak inflection point at $\eta \sim 1$, and for the larger boundary-layer thickness cases, the KTV data are able to bear this inflection point out; however, improvements to the SNR would have to be made to do this reliably at all conditions.

In Figs. 11 and 12, we are able to resolve the velocity very close to the wall, down to $y \sim 50$ $\mu$m. The SNR is appropriate for velocity profile extraction in all cases. We note that within the boundary layer, the SNR decreases because of the deformation of the tagged line due to the shear stress. This decrease in signal makes boundary-layer measurements notably more difficult than freestream measurements, which is consistent with past experience [73]. This means that boundary-layer measurements require higher laser power than freestream measurements. Furthermore, the write and read line thicknesses are nominally equal (approximately 300 $\mu$m), which is consistent with past KTV experiments in Fig. 6 of Zahradka *et al.* [72]. This indicates that there is minimal thermal expansion due to rapid gas heating from the write-laser pulse. More precisely, this experimental method imparts minimal perturbations to the sensitive laminar boundary-layer during measurement.

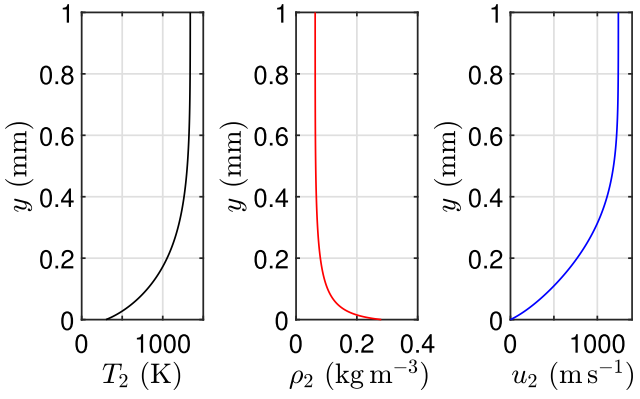


FIG. 10. Representative temperature, density, and velocity profiles calculated from the similarity solution. Conditions correspond to shot 169 in Table V.

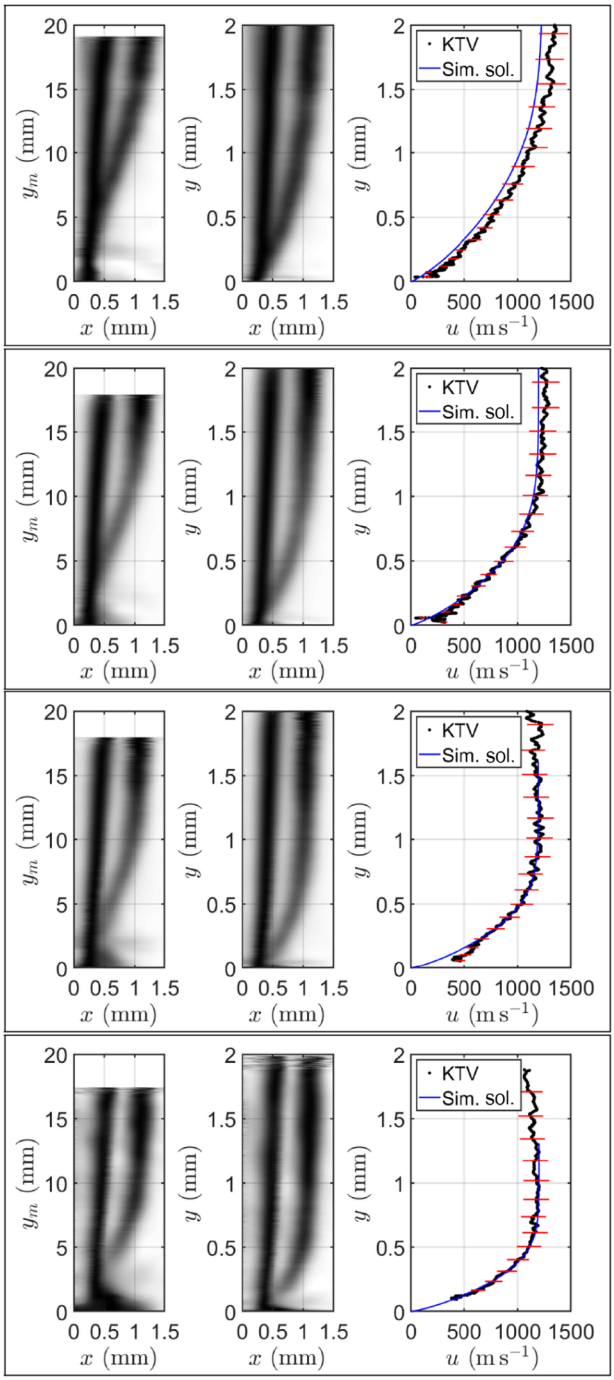


FIG. 11. Results for KTV experiments in 75% $N_2$/20% $O_2$/5% Kr. From the top, $Re_2^{\text{unit}} = 1.55 \times 10^5$ m$^{-1}$ (shot 163), $Re_2^{\text{unit}} = 3.80 \times 10^5$ m$^{-1}$ (shot 162), $Re_2^{\text{unit}} = 7.63 \times 10^5$ m$^{-1}$ (shot 159), $Re_2^{\text{unit}} = 1.15 \times 10^6$ m$^{-1}$ (shot 157). Left: Superposition of raw write and read KTV images (inverted scale). Center: Superposition of write and read images mapped from $y_m$ to $y$ (black). Right: Similarity solution in blue and KTV derived velocity profile in black with error bars in red.

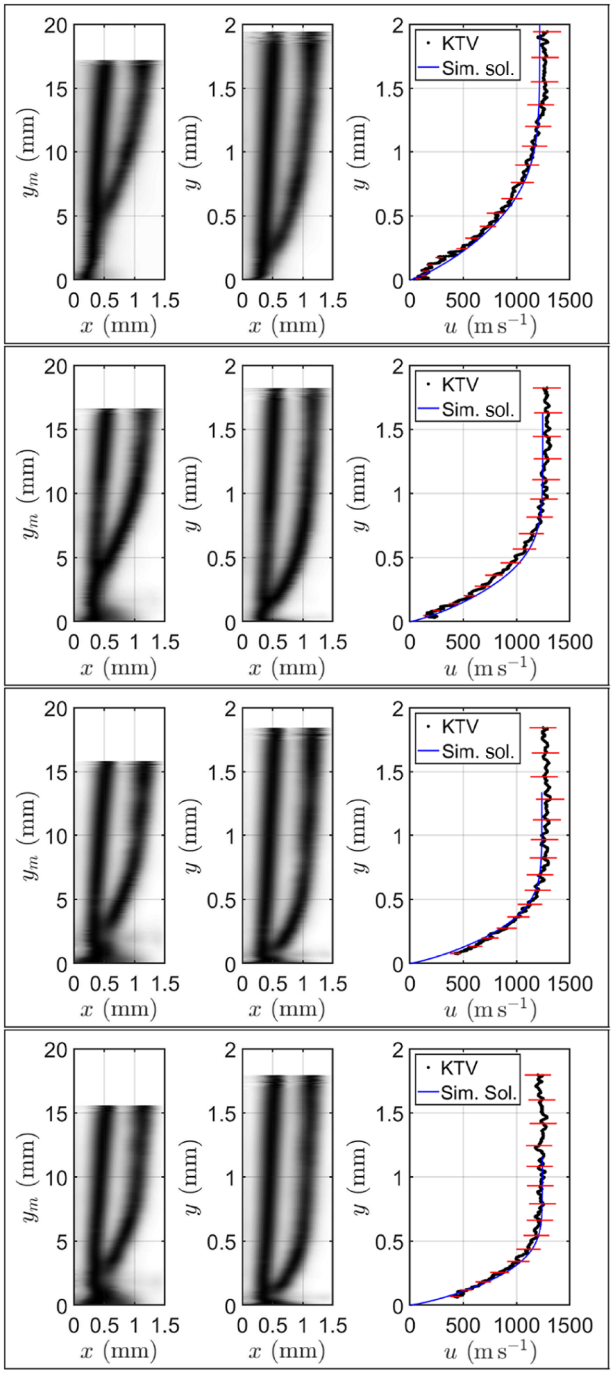


FIG. 12. Results for KTV experiments in 99% $N_2$/1%. From the top, $Re_2^{\text{unit}} = 3.88 \times 10^5$ m$^{-1}$ (shot 165), $Re_2^{\text{unit}} = 7.68 \times 10^5$ m$^{-1}$ (shot 166), $Re_2^{\text{unit}} = 1.15 \times 10^6$ m$^{-1}$ (shot 168), $Re_2^{\text{unit}} = 1.53 \times 10^6$ m$^{-1}$ (shot 159). Left: Superposition of raw write and read KTV images (inverted scale). Center: Superposition of write and read images mapped from $y_m$ to $y$ (black). Right: Similarity solution in blue and KTV derived velocity profile in black with error bars in red.

The signal count at the read step as a function of static pressure, $P_2$, for the air and $N_2$ mixtures is presented in Fig. 14. Initially, with increasing pressure, SNR in both

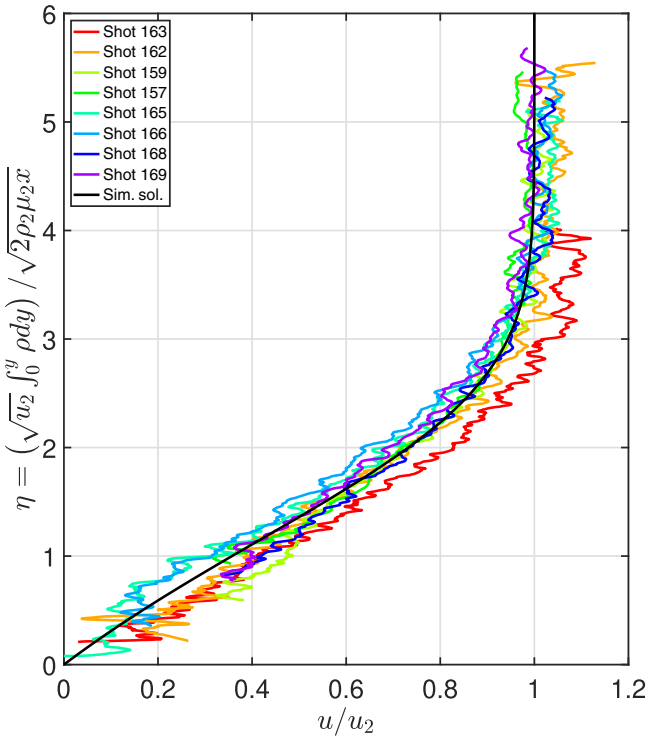


FIG. 13. Collapse of KTV derived velocity profiles and comparison to the similarity solution for compressible boundary-layer flow.

mixtures increases due to the increased krypton density. However, with increasing pressure, there is a trade-off between the increase in SNR due to higher krypton density and the decrease in SNR associated with the quenching of the excited tagged line. The increase in krypton density is initially the dominant effect up to a critical point, 12 kPa for $N_2$ and 6 kPa for air in these experiments. After this, the SNR starts to decrease with increasing pressure, indicating that the quenching effect is overtaking the effect of larger

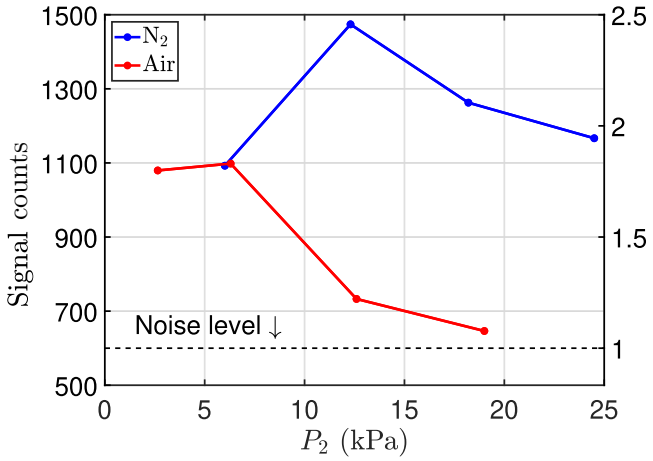


FIG. 14. Read step signal count vs static pressure, $P_2$, in air and $N_2$ mixtures at the boundary layer edge.

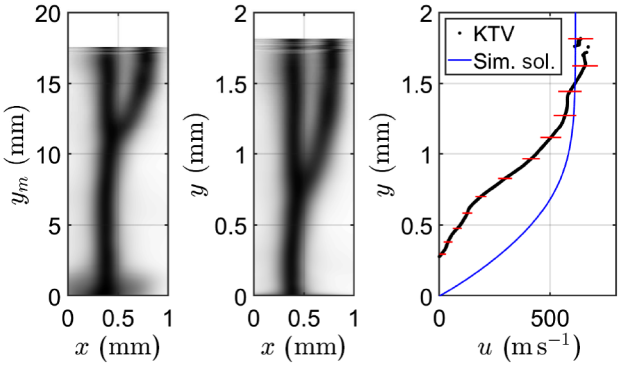


FIG. 15. Example of nonestablished flow in 99% $N_2$/1% Kr. Left: Superposition of raw write and read KTV images. Center: Superposition of write and read images mapped from $y_m$ to $y$. Right: Similarity solution in blue and KTV derived velocity profile in black with error bars in red.

krypton density. Additionally, we can see that, in Fig. 14, measurements could have been made at higher static pressure, $P_2$, for the $N_2$ experiments, but the Stevens shock tube could not produce these conditions.

## VIII. UTILITY OF OFF-SURFACE MEASUREMENTS

In this section, we present an example where off-surface measurements capture flow features that would otherwise be difficult to glean by surface measurements of pressure, temperature, or heat transfer. Figure 15 shows the results of an experiment in the Stevens shock tube performed with an air driver and a driven section of 99% $N_2$/1% Kr, where the postshock conditions are $P_2 = 4.7$ kPa, $T_2 = 635$ K, $u_2 = 613$ ms$^{-1}$, and $M_2 = 1.2$. The KTV derived velocity profile clearly shows that the flow is not established over the hollow cylinder. The most likely reason is that the postshock Mach number, $M_2$, is not high enough to have an attached shock wave on the sharp-angled cut at the leading edge of the inner surface of the hollow cylinder. This nonestablished flow is part of the reason why we choose to use a helium driver for the experiments presented in Sec. VII. Using a helium driver increases $M_2$ such that the shock wave over the sharp-angled cut on the inner surface is attached; as such, the flow over the hollow cylinder is quickly established and we are able to seek comparison to the similarity solutions. Surface measurements may have more difficulty identifying this behavior. Consequently, to determine whether the flow has been established in an experiment, especially in impulse facilities, off-surface measurements are invaluable.

## IX. CONCLUSIONS

A single-laser Krypton tagging velocimetry setup is used to study the quasisteady flow behind the primary shock wave over a hollow cylinder in the Stevens shock tube. The $(2 + 1)$ resonance-enhanced, multiphoton ionization (REMPI) of Kr with an excitation wavelength of $\lambda = 212.6$ nm is used to create the tracer whose fluorescence is imaged at successive times.

Relative to previous two-laser KTV schemes, this single-laser approach has the advantage of being simpler and more cost effective but has a higher laser-energy requirement. Emission spectra and the time-resolved fluorescence data are presented to support the assertion that the lifetime of the fluorescence signal is extended beyond the spontaneous emission timescale because the write-laser pulse is intense enough to partially ionize the Kr. The resulting recombination process occurs on a relatively slow timescale (approximately 1 $\mu$s), thus enabling a single-laser KTV technique. The choice of excitation wavelength is justified by two-photon absorption cross-section calculations.

KTV derived velocity profiles are recorded over a sectioned, sharp-edged hollow cylinder by propagating the write-laser beam tangentially to the cylinder surface. These results are then mapped to wall-normal locations corresponding to a flat plate for comparison to similarity solutions for a compressible, laminar boundary layer. Agreement between the similarity solutions and the KTV derived data is excellent in all cases.

Eight experiments are performed in two gas mixtures: (a) 99% $N_2$/1% Kr at postshock temperature $T_2 = 1300$ K, pressure range $P_2 = 6.0$–25 kPa, and unit Reynolds number range $Re_2 = 3.9 \times 10^5$ to $1.54 \times 10^6$ m$^{-1}$ and (b) in 75% $N_2$/20% $O_2$/5% Kr at postshock temperature $T_2 = 1400$ K, pressure range $P_2 = 2.7$–19 kPa, and unit Reynolds number range $Re_2 = 1.56 \times 10^5$ to $1.15 \times 10^6$ m$^{-1}$. Notably, the range of static conditions spans those typical of large-scale, high-enthalpy hypersonic impulse facilities, albeit at lower total enthalpy; that is, the freestream pressure and temperature (but not the velocity) of large-scale facilities are reproduced to demonstrate KTV utility.

Additionally, we present an example where the KTV derived velocity profile clearly shows that the flow is not established over the hollow cylinder. We come to the conclusion that the postshock Mach number, $M_2$, is not high enough to have an attached shock wave on the sharp-angled cut at the leading edge of the inner surface of the hollow cylinder. This is a demonstration that off-surface measurements, like KTV, capture flow features that would otherwise be difficult to obtain by surface measurements alone, especially in impulse facilities.

Challenges and limitations associated with this measurement technique include experiment timing, laser-energy requirements, and surface ablation. As is the case in impulse facilities, the short test time (approximately 1 ms) requires the use of a complex timing circuit that delays and subsequently triggers the laser pulse upon arrival of the

primary shock wave. The comparatively large laser-energy requirement is crucial to this technique, as it relies on using ionized Kr as the tracer particles. This requirement precludes tagging multiple lines in the flow, as splitting the laser beam would result in insufficient energy per line. Furthermore, the use of this technique in air at pressures higher than 19 kPa requires more than the 10 mJ/pulse currently possible with this laser system. The ablation of the model presents a challenge in that the resulting plume near the surface obscures the desired tagged line. Therefore, measurements where the laser-beam-model-grazing strategy is not employed would be more difficult.

The next step is to implement KTV in a large-scale, high-enthalpy impulse hypersonic facility. We should note that because of the way that error is handled in tagging velocimetry [Eq. (17)], the uncertainty would be reduced in high-enthalpy impulse facilities where the velocity is significantly higher. There are experimental timing issues with a conventional 10-Hz Nd:YAG/dye-laser setup like the one used in this work. However, advanced laser technology might serve to alleviate this concern, in addition to significantly increasing the repetition rate. Data in the literature suggest that the write step could be performed by ultrafast lasers [88] or a tunable form of a burst-mode laser [90]. Furthermore, the use of such lasers will enable us to reach converged statistics when studying unsteady flows in impulse facilities. For example, given a laser with a 10-kHz repetition rate, we would be able to acquire 500 samples in approximately 100 ms, which is the typical test time of Ludweig tubes. With a 100-kHz repetition rate, the required test time would be approximately 10 ms, which is typical of shock tunnels.

## ACKNOWLEDGMENTS

M.A.M. and N.J.P. are supported by AFOSR Young Investigator Program Grant No. FA9550-16-1-0262 and equipment for this work is supported by AFOSR DURIP Grant No. FA9550-15-1-0325; Ivett Leyva of AFOSR is the Program Manager for both grants. Support is also provided by U.S. Air Force Small Business Innovation Research Grants No. FA9101-17-P-0094 and No. FA2487-19-C-0013. D.S. is supported by the Stevens Institute of Technology Provost Fellowship. We would also like to acknowledge the machine work done by Bruce Fraser of the Stevens Institute of Technology.

[1] P. M. Danehy, J. Weisberger, C. Johansen, D. Reese, T. Fahringer, N. J. Parziale, C. Dedic, J. Estevadeordal, and B. A. Cruden, in *Flow Characterization and Modeling of Hypersonic Wind Tunnels (NATO Science and Technology Organization STO-AVT 325)* (Von Karman Institute, Brussels, Belgium, 2018).

[2] S. J. Beresh, J. F. Henfling, R. W. Spillers, and S. M. Spitzer, Postage-stamp PIV: Small velocity fields at 400 khz for turbulence spectra measurements, Meas. Sci. Technol. **29**, 034011 (2017).

[3] F. Scarano, in *Particle Image Velocimetry: New Developments and Recent Applications* (Springer Berlin Heidelberg, Berlin, Heidelberg, 2008), p. 445.

[4] E. Loth, Compressibility and rarefaction effects on drag of a spherical particle, AIAA J. **46**, 2219 (2008).

[5] D. Ragni, F. Schrijer, B. W. van Oudheusden, and F. Scarano, Particle tracer response across shocks measured by PIV, Exp. Fluids **50**, 53 (2011).

[6] G. E. Elsinga and G. C. Orlicz, Particle imaging through planar shock waves and associated velocimetry errors, Exp. Fluids **56**, 129 (2015).

[7] D. Mitchell, D. Honnery, and J. Soria, Particle relaxation and its influence on the particle image velocimetry cross-correlation function, Exp. Fluids **51**, 933 (2011).

[8] O. J. H. Williams, T. Nguyen, A.-M. Schreyer, and A. J. Smits, Particle response analysis for particle image velocimetry in supersonic flows, Phys. Fluids **27**, 076101 (2015).

[9] K. T. Lowe, Gwibo Byun, and R. L. Simpson, in *Proceedings of AIAA SciTech 2014* (AIAA-2014-0233, National Harbor, Maryland, 2014).

[10] J. M. Brooks, A. K. Gupta, M. S. Smith, and E. C. Marineau, Particle image velocimetry measurements of Mach 3 turbulent boundary layers at low Reynolds numbers, Exp. Fluids **59**, 83 (2018).

[11] M. M. Koochesfahani and D. G. Nocera, in *Springer Handbook of Experimental Fluid Mechanics*, edited by C. Tropea, A. L. Yarin, and J. F. Foss (Springer, 2007).

[12] J. Haertig, M. Havermann, C. Rey, and A. George, Particle image velocimetry in Mach 3.5 and 4.5 shock-tunnel flows, AIAA J. **40**, 1056 (2002).

[13] A. G. Hsu, R. Srinivasan, R. D. W. Bowersox, and S. W. North, Molecular tagging using vibrationally excited nitric oxide in an underexpanded jet flowfield, AIAA J. **47**, 2597 (2009).

[14] A. G. Hsu, R. Srinivasan, R. D. W. Bowersox, and S. W. North, Two-component molecular tagging velocimetry utilizing NO fluorescence lifetime and $NO_2$ photodissociation techniques in an underexpanded jet flowfield, Appl. Opt. **48**, 4414 (2009).

[15] R. Sánchez-González, R. Srinivasan, R. D. W. Bowersox, and S. W. North, Simultaneous velocity and temperature measurements in gaseous flow fields using the venom technique, Opt. Lett. **36**, 196 (2011).

[16] R. Sánchez-González, R. D. W. Bowersox, and S. W. North, Simultaneous velocity and temperature measurements in gaseous flow fields using the vibrationally excited nitric oxide monitoring technique: A comprehensive study, Appl. Opt. **51**, 1216 (2012).

[17] R. Sánchez-González, R. D. W. Bowersox, and S. W. North, Vibrationally excited NO tagging by $NO(A^2\Sigma^+)$ fluorescence and quenching for simultaneous velocimetry and thermometry in gaseous flows, Opt. Lett. **39**, 2771 (2014).

[18] N. Dam, R. J. H. Klein-Douwel, N. M. Sijtsema, and J. J. ter Meulen, Nitric oxide flow tagging in unseeded air, Opt. Lett. **26**, 36 (2001).

[19] N. M. Sijtsema, N. J. Dam, R. J. H. Klein-Douwel, and J. J. ter Meulen, Air photolysis and recombination tracking: A new molecular tagging velocimetry scheme, AIAA J. **40**, 1061 (2002).
[20] W. P. N. Van der Laan, R. A. L. Tolboom, N. J. Dam, and J. J. ter Meulen, Molecular tagging velocimetry in the wake of an object in supersonic flow, Exp. Fluids **34**, 531 (2003).
[21] R. Miles, C. Cohen, J. Connors, P. Howard, S. Huang, E. Markovitz, and G. Russell, Velocity measurements by vibrational tagging and fluorescent probing of oxygen, Opt. Lett. **12**, 861 (1987).
[22] R. B. Miles, J. J. Connors, E. C. Markovitz, P. J. Howard, and G. J. Roth, Instantaneous profiles and turbulence statistics of supersonic free shear layers by Raman excitation pluslaser-induced electronic fluorescence (RELIEF) velocity tagging of oxygen, Exp. Fluids **8**, 17 (1989).
[23] R. B. Miles, D. Zhou, B. Zhang, and W. R. Lempert, Fundamental turbulence measurements by RELIEF flow tagging, AIAA J. **31**, 447 (1993).
[24] R. B. Miles and W. R. Lempert, Quantitative flow visualization in unseeded flows, Annu. Rev. Fluid Mech. **29**, 285 (1997).
[25] R. B. Miles, J. Grinstead, R. H. Kohl, and G. Diskin, The RELIEF flow tagging technique and its application in engine testing facilities and for helium-air mixing studies, Meas. Sci. Technol. **11**, 1272 (2000).
[26] J. B. Michael, M. R. Edwards, A. Dogariu, and R. B. Miles, Femtosecond laser electronic excitation tagging for quantitative velocity imaging in air, Appl. Opt. **50**, 5158 (2011).
[27] M. R. Edwards, A. Dogariu, and R. B. Miles, Simultaneous temperature and velocity measurements in air with femtosecond laser tagging, AIAA J. **53**, 2280 (2015).
[28] N. Jiang, B. R. Halls, H. U. Stauffer, P. M. Danehy, J. R. Gord, and S. Roy, Selective two-photon absorptive resonance femtosecond-laser electronic-excitation tagging velocimetry, Opt. Lett. **41**, 2225 (2016).
[29] N. Jiang, J. G. Mance, M. N. Slipchenko, J. J. Felver, H. U. Stauffer, T. Yi, P. M. Danehy, and S. Roy, Seedless velocimetry at 100 khz with picosecond-laser electronic-excitation tagging, Opt. Lett. **42**, 239 (2017).
[30] P. M. Danehy, P. Mere, M. J. Gaston, S. O'Byrne, P. C. Palma, and A. F. P. Houwing, Fluorescence velocimetry of the hypersonic, separated flow over a cone, AIAA J. **39**, 1320 (2001).
[31] P. M. Danehy, S. O'Byrne, A. F. P. Houwing, J. S. Fox, and D. R. Smith, Flow-tagging velocimetry for hypersonic flows using fluorescence of nitric oxide, AIAA J. **41**, 263 (2003).
[32] J. Bominaar, M. Pashtrapanska, T. Elenbaas, N. Dam, H. Ter Meulen, and W. van de Water, Writing in turbulent air, Phys. Rev. E **77**, 046312 (2008).
[33] B. F. Bathel, P. M. Danehy, J. A. Inman, S. B. Jones, C. B. Ivey, and C. P. Goyne, Velocity profile measurements in hypersonic flows using sequentially imaged fluorescence-based molecular tagging, AIAA J. **49**, 1883 (2011).
[34] P. Matos, L. G. Barreta, and C. A. Martins, Velocity and NO-lifetime measurements in an unseeded hypersonic air flow, J. Fluids Eng. **140**, 121105 (2018).
[35] J. L. Mills, Ph.D. thesis, Old Dominion University, 2016.
[36] J. C. McDaniel, B. Hiller, and R. K. Hanson, Simultaneous multiple-point velocity measurements using laser-induced iodine fluorescence, Opt. Lett. **8**, 51 (1983).
[37] R. J. Balla, Iodine tagging velocimetry in a Mach 10 wake, AIAA J. **51**, 1783 (2013).
[38] P. Barker, A. Bishop, and H. Rubinsztein-Dunlop, Supersonic velocimetry in a shock tube using laser enhanced ionisation and planar laser induced fluorescence, Appl. Phys. B **64**, 369 (1997).
[39] W. R. Lempert, N. Jiang, S. Sethuram, and M. Samimy, Molecular tagging velocimetry measurements in supersonic microjets, AIAA J. **40**, 1065 (2002).
[40] W. R. Lempert, M. Boehm, N. Jiang, S. Gimelshein, and D. Levin, Comparison of molecular tagging velocimetry data and direct simulation monte carlo simulations in supersonic micro jet flows, Exp. Fluids **34**, 403 (2003).
[41] T. Handa, K. Mii, T. Sakurai, K. Imamura, S. Mizuta, and Y. Ando, Study on supersonic rectangular microjets using molecular tagging velocimetry, Exp. Fluids **55**, 1 (2014).
[42] S. Zhang, X. Yu, H. Yan, H. Huang, and H. Liu, Molecular tagging velocimetry of NH fluorescence in a high-enthalpy rarefied gas flow, Appl. Phys. B **123**, 122 (2017).
[43] L. R. Boedeker, Velocity measurement by $H_2O$ photolysis and laser-induced fluorescence of OH, Opt. Lett. **14**, 473 (1989).
[44] J. A. Wehrmeyer, L. A. Ribarov, D. A. Oguss, and R. W. Pitz, Flame flow tagging velocimetry with 193-nm $H_2O$ photodissociation, Appl. Opt. **38**, 6912 (1999).
[45] R. W. Pitz, M. D. Lahr, Z. W. Douglas, J. A. Wehrmeyer, S. Hu, C. D. Carter, K.-Y. Hsu, C. Lum, and M. M. Koochesfahani, Hydroxyl tagging velocimetry in a supersonic flow over a cavity, Appl. Opt. **44**, 6692 (2005).
[46] M. A. André, P. M. Bardet, R. A. Burns, and P. M. Danehy, Characterization of hydroxyl tagging velocimetry for low-speed flows, Meas. Sci. Technol. **28**, 085202 (2017).
[47] B. Hiller, R. A. Booman, C. Hassa, and R. K. Hanson, Velocity visualization in gas flows using laser-induced phosphorescence of biacetyl, Rev. Sci. Instrum. **55**, 1964 (1984).
[48] C. P. Gendrich and M. M. Koochesfahani, A spatial correlation technique for estimating velocity fields using molecular tagging velocimetry (MTV), Exp. Fluids **22**, 67 (1996).
[49] C. P. Gendrich, M. M. Koochesfahani, and D. G. Nocera, Molecular tagging velocimetry and other novel applications of a new phosphorescent supramolecule, Exp. Fluids **23**, 361 (1997).
[50] B. Stier and M. M. Koochesfahani, Molecular tagging velocimetry (MTV) measurements in gas phase flows, Exp. Fluids **26**, 297 (1999).
[51] L. A. Ribarov, J. A. Wehrmeyer, F. Batliwala, R. W. Pitz, and P. A. DeBarber, Ozone tagging velocimetry using narrowband excimer lasers, AIAA J. **37**, 708 (1999).
[52] M. A. André, R. A. Burns, P. M. Danehy, S. R. Cadell, B. G. Woods, and P. M. Bardet, Development of $N_2O$-MTV for low-speed flow and in-situ deployment to an integral effect test facility, Exp. Fluids **59**, 14 (2018).

[53] F. K. Lu and D. E. Marren, *Advanced Hypersonic Test Facilities* (AIAA, Reston, Virginia, 2002).
[54] H. G. Hornung, in *Proceedings of the First Pacific International Conference on Aerospace Science and Technology* (Taiwan, 1993).
[55] J. Belanger and H. G. Hornung, Transverse jet mixing and combustion experiments in hypervelocity flows, J. Propul. Power **12**, 186 (1996).
[56] C. Y. Wen and H. G. Hornung, Non-equilibrium dissociating flow over spheres, J. Fluid Mech. **299**, 389 (1995).
[57] P. H. Adam and H. G. Hornung, Enthalpy effects on hypervelocity boundary-layer transition: Ground test and flight data, J. Spacecr. Rockets **34**, 614 (1997).
[58] K. Fujii and H. G. Hornung, Experimental investigation of high-enthalpy effects on attachment-line boundary-layer transition, AIAA J. **41**, 1282 (2003).
[59] N. J. Parziale, J. E. Shepherd, and H. G. Hornung, Differential interferometric measurement of instability in a hypervelocity boundary layer, AIAA J. **51**, 750 (2013).
[60] N. J. Parziale, J. E. Shepherd, and H. G. Hornung, Free-stream density perturbations in a reflected-shock tunnel, Exp. Fluids **55**, 1665 (2014).
[61] N. J. Parziale, J. E. Shepherd, and H. G. Hornung, Observations of hypervelocity boundary-layer instability, J. Fluid Mech. **781**, 87 (2015).
[62] P. D. Germain and H. G. Hornung, Transition on a slender cone in hypervelocity flow, Exp. Fluids **22**, 183 (1997).
[63] J. S. Jewell, Ph.D. thesis, California Institute of Technology, 2014.
[64] J. S. Jewell, N. J. Parziale, I. A. Leyva, and J. E. Shepherd, Effects of shock-tube cleanliness on hypersonic boundary layer transition at high enthalpy, AIAA J. **55**, 332 (2017).
[65] M. Havermann, J. Haertig, C. Rey, and A. George, in *Particle Image Velocimetry: New Developments and Recent Applications* (Springer Berlin Heidelberg, Berlin, Heidelberg, 2008), p. 429.
[66] J. L. Wagner, E. P. DeMauro, K. M. Casper, S. J. Beresh, K. P. Lynch, and B. O. Pruett, Pulse-burst PIV of an impulsively started cylinder in a shock tube for Re > 105, Exp. Fluids **59**, 106 (2018).
[67] A. A. Martinez, G. C. Orlicz, and K. P. Prestridge, A new experiment to measure shocked particle drag using multi-pulse particle image velocimetry and particle tracking, Exp. Fluids **56**, 1854 (2015).
[68] A. N. Perkins, M. Ramsey, and R. W. Pitz, in *49th AIAA Aerospace Sciences Meeting including the New Horizons Forum and Aerospace Exposition, Aerospace Sciences Meetings* (AIAA-2011-1092, Orlando, FL, USA, 2011).
[69] J. L. Mills, C. I. Sukenik, and R. J. Balla, in *Proceedings of 42nd AIAA Plasmadynamics and Lasers Conference* (AIAA 2011-3459, Honolulu, Hawaii, 2011).
[70] R. J. Balla and J. L. Everhart, Rayleigh scattering density measurements, cluster theory, and nucleation calculations at Mach 10, AIAA J. **50**, 698 (2012).
[71] N. J. Parziale, M. S. Smith, and E. C. Marineau, Krypton tagging velocimetry of an underexpanded jet, Appl. Opt. **54**, 5094 (2015).
[72] D. Zahradka, N. J. Parziale, M. S. Smith, and E. C. Marineau, Krypton tagging velocimetry in a turbulent mach 2.7 boundary layer, Exp. Fluids **57**, 62 (2016).
[73] M. A. Mustafa, N. J. Parziale, M. S. Smith, and E. C. Marineau, Amplification and structure of streamwise-velocity fluctuations in compression-corner shock-wave/turbulent boundary-layer interactions, J. Fluid Mech. **863**, 1091 (2019).
[74] M. A. Mustafa, N. J. Parziale, M. S. Smith, and E. C. Marineau, Nonintrusive freestream velocity measurement in a large-scale hypersonic wind tunnel, AIAA J. **55**, 3611 (2017).
[75] M. A. Mustafa and N. J. Parziale, Simplified read schemes for krypton tagging velocimetry in $N_2$ and air, Opt. Lett. **43**, 2909 (2018).
[76] O. Echt, M. C. Cook, and A. W. Castleman, Krypton dimers: Resonance-enhanced MPI via gerade states in the region of atomic $4p^5 5p$ configurations, J. Chem. Phys. **87**, 3276 (1987).
[77] M. D. Perry and O. L. Landen, Resonantly enhanced multiphoton ionization of krypton and xenon with intense ultraviolet laser radiation, Phys. Rev. A **38**, 2815 (1988).
[78] J. C. Miller, Two-photon resonant multiphoton ionization and stimulated emission in krypton and xenon, Phys. Rev. A **40**, 6969 (1989).
[79] S. J. Bajic, R. N. Compton, X. Tang, and P. Lambropoulos, Resonantly enhanced multiphoton-ionization photoelectron spectroscopy of krypton and xenon: Experiment and theory, Phys. Rev. A **44**, 2102 (1991).
[80] F. Brandi, W. Hogervorst, and W. Ubachs, High-resolution vacuum-ultraviolet and ultraviolet photoionization spectroscopy of krypton, J. Phys. B: Atom. Mol. Opt. Phys. **35**, 1071 (2002).
[81] Y. Shiu and M. A. Biondi, Dissociative Recombination in Krypton: Dependence of the Total Rate Coefficient and Excited-state Production on Electron Temperature, Phys. Rev. Appl. **16**, 1817 (1977).
[82] M. A. Dakka, G. Tsiminis, R. D. Glover, C. Perrella, J. Moffatt, N. A. Spooner, R. T. Sang, P. S. Light, and A. N. Luiten, Laser-based Metastable Krypton Generation, Phys. Rev. Lett. **121**, 093201 (2018).
[83] A. G. Hsu, V. Narayanaswamy, N. T. Clemens, and J. H. Frank, Mixture fraction imaging in turbulent non-premixed flames with two-photon LIF of krypton, Proc. Combust. Inst. **33**, 759 (2011).
[84] A. C. Eckbreth, *Laser Diagnostics for Combustion Temperature and Species* (Gordon and Breach Publications, Amsterdam, The Netherlands, 1996), 2nd ed.
[85] P. Lambropoulos, Topics on multiphoton processes in atoms, Adv. Atom. Mol. Phys. **12**, 87 (1976).
[86] N. M. Khambatta, J. A. Oertel, R. Silk, L. J. Radziemski, and J. M. Mack, Absolute excited state and ion densities from two-and three-photon processes in some 6p levels of atomic krypton, J. Appl. Phys. **64**, 4809 (1988).
[87] N. M. Khambatta, L. J. Radziemski, and S. N. Dixit, Upper bound fora three-photon excitation cross section in atomic argon in the ultraviolet regime, Phys. Rev. A **39**, 3842 (1989).
[88] D. R. Richardson, N. Jiang, H. U. Stauffer, S. P. Kearney, S. Roy, and J. R. Gord, Mixture-fraction imaging at 1 kHz

using femtosecond laser-induced fluorescence of krypton, Opt. Lett. **42**, 3498 (2017).

[89] J. Bokor, J. Y. Zavelovich, and C. K. Rhodes, Multiphoton ultraviolet spectroscopy of some 6*p* levels in krypton, Phys. Rev. A **21**, 1453 (1980).

[90] M. N. Slipchenko, J. D. Miller, S. Roy, J. R. Gord, S. A. Danczyk, and T. R. Meyer, Quasi-continuous burst-mode laser for high-speed planar imaging, Opt. Lett. **37**, 1346 (2012).

[91] D. G. Goodwin, in *Proceedings of CVD XVI and EuroCVD Fourteen*, edited by M. Allendorf, F. Maury, and F. Teyssandier (Electrochemical Society, Pennington, N.J., 2003), p. 155.

[92] S. Browne, J. Ziegler, and J. E. Shepherd, *Numerical Solution Methods for Shock and Detonation Jump Conditions*, GALCIT -FM2006-006 (2006).

[93] F. White, *Viscous Fluid Flow* (McGraw-Hill, New York, NY, 2006), 3rd ed.

[94] J. J. Kuehl, Thermoacoustic interpretation of second-mode instability, AIAA J. **56**, 3585 (2018).

[95] T. O'Haver, *A pragmatic introduction to signal processing* (University of Maryland at College Park, College Park, Maryland, 1997).

[96] R. B. Hill and J. C. Klewicki, Data reduction methods for flow tagging velocity measurements, Exp. Fluids **20**, 142 (1996).